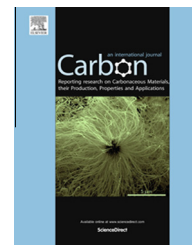


Available at www.sciencedirect.com

ScienceDirect

journal homepage: www.elsevier.com/locate/carbon

Quantitative 2D electrooxidative carbon nanotube filter model: Insight into reactive sites

Han Liu ^a, Jia Liu ^a, Yanbiao Liu ^{a,b}, Katia Bertoldi ^a, Chad D. Vecitis ^{a,*}

^a School of Engineering and Applied Sciences, Harvard University, 29 Oxford Street, Cambridge, MA 02138, United States

^b Department of Civil and Environmental Engineering, Faculty of Engineering, National University of Singapore, 1 Engineering Drive 2, E1A-07-03, Singapore 117576, Singapore

ARTICLE INFO

Article history:

Received 18 March 2014

Accepted 3 September 2014

Available online 15 September 2014

ABSTRACT

In this study, the electrooxidative carbon nanotube (CNT) filtration of sorptive methyl orange (MO) and non-sorptive ferrocyanide was investigated by both experiment and numerical simulation. The two-dimensional numerical model includes target molecule; mass transport, adsorption, and electron transfer and product desorption. For MO, the model was calibrated with experimental reaction rates from the mass- and electron-transfer limited regimes and accurately predicted effluent concentrations over a much larger range of conditions. For ferrocyanide, five CNT electrodes of various specific surface area and surface oxygen content were utilized and a similar single reaction site model to MO accurately predicted kinetics at low anode potentials while a two-site model was necessary at higher potentials yielding insight into the CNT reactive sites. For example, at low anode potentials (≤ 0.2 V), the kinetics have a linear correlation with CNT surface area indicating the sp^2 conjugated sidewall sites are dominant. In contrast, at higher anode potentials (≥ 0.3 V), the kinetics were significantly greater than expected from CNT surface area and the differential kinetics have a linear correlation with the CNT surface oxygen content indicating the CNT tips were also electroactive. The spatial distribution of internal electrode mass transport and surface reactivity is discussed.

© 2014 Elsevier Ltd. All rights reserved.

1. Introduction

Electrochemical filtration has great potential for a number of applications such as advanced microbial, gas, and water separations. For example, electrochemical filtration has been reported to be effective towards oxidation of organics and ions [1,2] and inactivation of virus (MS2) and bacteria (*Escherichia coli*) [3,4], and can be coupled with microbiology [5] or hydrolysis [6] to enhance pollutant degradation. The electrochemistry and filtration are synergistic as the fluid flow through the electrode can increase electrochemical kinetics by over 10-fold [7] and the electric field can enhance

electroosmotic flow efficiency by over 100-fold [8]. Elemental carbon-based materials such as carbon cloths or felts have been classically utilized as electrochemical filters [9]. Recently, carbon nanotubes (CNT) have drawn attention as electrochemical filters [10] due to their unique combination of conductivity, chemical stability, and ability to form high porosity networks. Many current research studies are focused on improving our fundamental understanding of the individual processes that mediate the overall performance of an electrochemical CNT filter.

Qualitatively, the reactive transport mechanism describing Faradaic electrochemical CNT filtration has four primary

* Corresponding author.

E-mail address: vecitis@seas.harvard.edu (C.D. Vecitis).

<http://dx.doi.org/10.1016/j.carbon.2014.09.009>

0008-6223/© 2014 Elsevier Ltd. All rights reserved.

steps: target molecule mass transport, adsorption, and electron transfer and product desorption, with the flow through the electrode significantly increasing mass transport and product desorption [11]. However, an in-depth understanding of the effect of target molecule & CNT physical-chemical properties requires not only a qualitative, but also a quantitative understanding of the aforementioned mechanisms. For example, there is a vast number of aqueous electrochemical target molecules ranging from inorganics such as nitrite [12], halides [2], and heavy metals [13,14] to organics such as aromatics [15] and biomolecules [16,17] that significantly differ in physical-chemical properties. There are also a wide range of CNT [18] in terms of diameter that will affect surface area and pore size [19], length that will affect number of reactive sites and network mechanical stability [20], and surface chemistry such as N/B-doping [21] or surface oxidation that will affect CNT conductivity and reactivity. Therefore, the development of a quantitative electrochemical filtration model would allow for a more rapid examination of the innumerable combinations of experimental conditions.

Quantitative electrochemistry modeling studies typically utilize simple reactors with controlled hydraulic convection [22–24] such as the rotating disk electrode (RDE) [25,26] where the homogenous flow pattern and concentration field can be analytically solved. For more complex and practical electrode configurations, numerical simulation will be necessary. For example, Zhang et al. [27] recently reported an experimental and simulation study of CO oxidation in a thin-layer flow cell using a reactive transport mechanism qualitatively similar to that for electrochemical filtration [11]. The experimental electrooxidative reaction current and CO concentration field were accurately simulated with both 2D and 3D models. Thus, a similar multi-dimensional model may be able to quantitatively simulate electrochemical CNT filtration.

In regards to the CNT characteristics that control electrochemical kinetics, the location and type of the CNT surface reactive sites are of particular interest. The two plausible major CNT reactive sites are (1) the sp^2 conjugated CNT sidewalls and (2) the surface oxy defect sites found predominantly at the CNT tips as displayed in Fig. 1. The prevailing

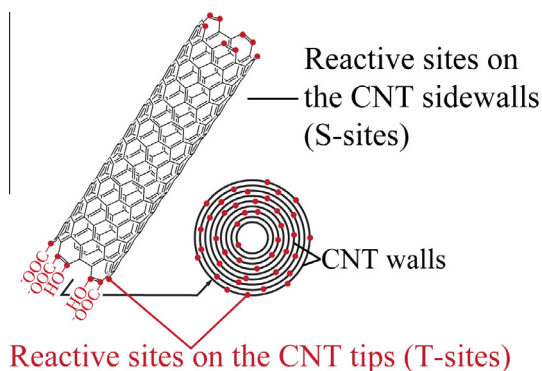


Fig. 1 – Schematic representation of the predominant CNT electro-active sites. CNT sp^2 conjugated sidewall sites (S-sites) versus CNT oxy-defect tip sites (T-sites). (A color version of this figure can be viewed online.)

hypothesis on CNT reactive sites is that the CNT sidewall is inert and the CNT tips with high oxy-functional group defect site density dominate electrochemistry, analogous to the inert basal plane and the reactive edge-steps of highly oriented pyrolytic graphite [28]. For example, cyclic voltammetry (CV) studies of epinephrine oxidation and ferricyanide reduction on a multiwall carbon nanotube electrode indicated the CNT tips were the predominant reactive sites [29]. However, a recent CV study observed that the oxygenated species formed on free-standing CNT tips after acid treatment did not measurably change the heterogeneous charge transfer kinetics [30]. Another CV study, in which either the CNT sidewall or tips were coated by insulating polystyrene reported that the CNT sidewalls were also active and that the location of the dominant electro-active site, sidewall versus tip, was a function of target molecule physical-chemical properties [31]. To date, CV has been the predominant electrochemical method to investigate the specific identity of CNT electro-active sites [28]. To fully explore the interplay of CNT tip versus sidewall electro-activity, there is a need for experimental methodologies that go beyond CV analysis [28]. Thus, investigations of the CNT reactive sites using experimental reaction rates from a randomly-oriented CNT network are needed and will require a quantitative electrochemical kinetics model to gain insight into reaction site identity.

In this study, we developed and validated a 2D quantitative electrochemical CNT filtration model that includes mass transport, adsorption, and electron transfer processes. The model is used to numerically simulate the electrooxidation kinetics of (1) methyl orange (MO), a sorptive species that undergoes a multi-electron transfer oxidation, and (2) ferrocyanide, a non-sorptive species that undergoes a single electron transfer oxidation. The electrooxidation filtration rate for both species was experimentally and numerically examined as a function of both the influent concentration (C_{in}) and anode potential (E). The ferrocyanide electrooxidation experiments and modeling was completed for five CNT anodes that are characterized in detail by scanning electron microscopy (SEM), transmission electron microscopy (TEM), BET specific surface area analysis (BET), and X-ray photoelectron spectroscopy (XPS). The CNT specific surface area and surface oxygen content dependent ferrocyanide electrooxidation kinetics are used to gain insight into the predominant CNT electro-active sites. The 2D electrochemical filtration model was used to gain insight into the microscopic target molecule concentration and convection-diffusion flux fields within the electrochemical CNT filter.

2. Experimental

2.1. Chemicals

Methyl orange hydrate (>95%), potassium hexacyanoferrate (II) trihydrate ($K_4Fe(CN)_6 \cdot 3H_2O$; 98.5–102.0%), and sodium sulfate (Na_2SO_4 ; >99%) were purchased from Sigma-Aldrich (St. Louis, MO). Methyl orange was quantified by its absorption at $\lambda_{max} = 464 \text{ nm}$ ($\epsilon = 26,900 \text{ M}^{-1} \text{ cm}^{-1}$) and ferrocyanide was quantified by its absorption at $\lambda_{max} = 420 \text{ nm}$ ($\epsilon = 1000 \text{ M}^{-1} \text{ cm}^{-1}$) using an Agilent 8453 UV-visible spectrophotometer.

2.2. Anodic CNT filter

In this study, we utilized multiwalled carbon nanotubes that had been made into preformed porous networks with an average depth of 64–96 μm (NanoTechLabs, Buckeye Composites, Yadinkville, NC). Five CNT types were used in this study are of different diameter, wall number, specific surface area, and oxygen content and are referred as A-CNT, B-CNT, C-CNT, D-CNT, and E-CNT. The A-CNT networks were used as the anode material in the MO kinetics study and all five CNT networks were used as anode materials in the ferrocyanide study.

2.3. CNT characterization

The five different multi-walled carbon nanotubes were characterized in detail by TEM, SEM, XPS, and BET to determine diameter (d), number of walls, surficial O/C ratio, and specific surface area. Characterization details can be found in the [Supporting information](#).

2.4. Electrochemical filtration

Sodium sulfate (Na_2SO_4) was utilized as the background electrolyte and methyl orange and ferrocyanide were used as the target molecules for electrochemical filtration. The sodium sulfate concentration was 0.1 M for methyl orange experiments and 1 M for ferrocyanide experiments to minimize the effects of electro-migration (<5% overall mass transport; calculations in [SI](#)). Influent solutions were peristaltically pumped (Masterflex) through the electrochemical CNT filter of area 7.06 cm^2 at 3.0 mL min^{-1} and the electrochemistry was driven by a CHI604D electrochemical workstation. A detailed description of the electrochemical filtration system has been previously reported [2] and a schematic and images of the apparatus are displayed in [Fig. S1](#). Before every experiment, the titanium ring was polished with sandpaper to optimize the electrical connectivity between the Ti and the CNT network. For all filtration experiments, effluent aliquots were collected after 180 s to ensure steady-state and the concentration was measured by UV-vis to calculate the electrooxidation rate.

3. CNT characterization

The five CNT networks were characterized by XPS to determine surface oxygen content, BET to determine specific surface area, and TEM to determine diameter distribution and number of walls. Representative TEM images of the A-CNT network and an individual A-CNT with a tube wall spacing of 0.33 nm are displayed in [Fig. 2a](#) and [b](#), respectively. Similar TEM images of the B-E CNT networks are displayed in [Fig. S2](#). The CNT diameter and wall number distribution were determined by TEM image analysis (ImageJ) and are summarized in [Table 1](#). The average CNT diameter ranged from 23.5 (A-CNT) to 93.3 nm (D-CNT) and the average number of walls ranged from 20 (A-CNT) to 119 (D-CNT) per nanotube with the number of walls increasing monotonically with CNT diameter. Since the CNT diameter distributions are variable, histograms of the CNT diameters and wall numbers are presented in [Figs. S3 and S4](#), respectively. The CNT XPS survey scans are displayed in [Fig. S5](#) and the CNT surface oxygen percentage is listed in [Table 1](#). The CNT surface oxygen atomic percentage ranged from 0.55% (A-CNT) to 2.16% (D-CNT) and the SSA ranged from 20.0 (D-CNT) to 88.5 $\text{m}^2 \text{g}^{-1}$ (A-CNT). The total surface areas (S) were calculated using the filter weight and SSA as summarized in [Table 1](#). The total CNT filter surface area ranged from 0.35 (D-CNT) to 1.47 m^2 (A-CNT). The CNT physical-chemical parameters are the basis for the model geometry design that will be discussed in detail later.

4. Methyl orange electrooxidative filtration kinetics

4.1. Modeling approach

4.1.1. Electrochemical CNT filter 2D model geometry

The A-CNT network (depth $\sim 83 \mu\text{m}$; $d_{\text{A-CNT}} = 23.4 \pm 7.3 \text{ nm}$) was used as the anode material for the methyl orange (MO) electrooxidation experiments. The model geometry consists of a 5- μm headspace followed by the 83- μm anodic CNT filter and another 5- μm space after the filter bed as shown in [Fig. 3a](#). An SEM image of the 83- μm CNT filter cross-section is presented in [Fig. 3b](#) and the thin ($\sim \mu\text{m}$) CNT layers stacked

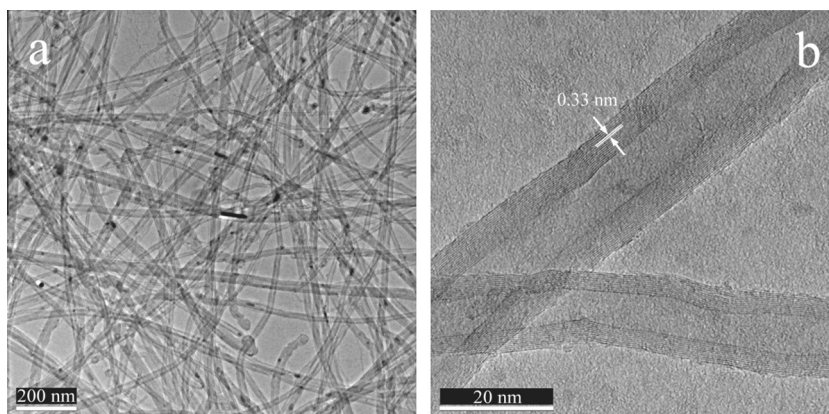


Fig. 2 – Representative TEM images of the A-CNT network. (a) Top view of the porous A-CNT network. (b) Magnified view of CNT network showing the spacing between two adjacent walls.

Table 1 – Physical–chemical characteristics of the CNT networks.

CNT	A	B	C	D	E
Diameter (nm)	23.4 ± 7.3	27.7 ± 17.1	71.4 ± 58.5	93.3 ± 69.5	36.0 ± 4.3
Number of walls	20 ± 11.5	32 ± 26	102 ± 93	119 ± 92	40 ± 5
Oxygen (%) ^a	0.55 ± 0.05	0.77 ± 0.24	1.06 ± 0.2	2.16 ± 0.15	1.55 ± 0.17
SSA (m ² g ⁻¹) ^b	88.5	34.6	30.3	20.0	55.9
Filter weight (mg)	17.1	22	21.2	17.5	19.2
S (m ²) ^c	1.47	0.76	0.64	0.35	1.07
Filter depth (μm)	83.0 ± 3.5	96.5 ± 4.2	88.8 ± 2.3	64.0 ± 4.0	92.3 ± 3.8

^a Surface oxygen content measured by XPS.
^b BET specific surface area.
^c Total surface area calculated by the weight of CNT networks × SSA.

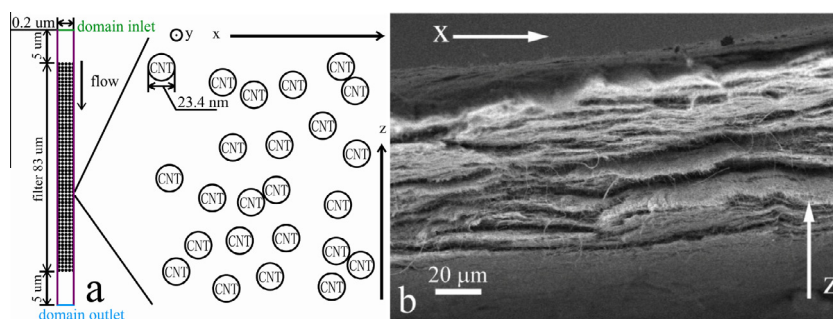


Fig. 3 – A-CNT network model geometry. (a) 2D CNT geometry used in numerical simulation where the CNT are assumed to be randomly distributed, of the same diameter, and the vertical cross-sections are assumed to be circles. Scheme includes the domain inlet (green), domain outlet (blue), periodic boundary on the left and right (purple) and CNT electrode surfaces (black). (b) Cross-sectional SEM image of the A-CNT network used for electrochemical filtration. (A color version of this figure can be viewed online.)

Table 2 – Governing equations and boundary conditions for hydraulics and species transport.

	Governing equations	Boundary conditions			
		CNT surface	Domain inlet	Domain outlet	Periodic
Hydraulic field	$\rho \frac{D\mathbf{u}}{Dt} = -\nabla p + \rho \mathbf{g} + \mu \nabla^2 \mathbf{u}$ $\nabla \cdot \mathbf{u} = 0$	$\mathbf{u} = 0$	$\mathbf{u} = u_{in}$	$P = P_0$ $\mu (\nabla \mathbf{u} + (\nabla \mathbf{u})^T) = 0$	$\mathbf{u}_{source} = \mathbf{u}_{dest}$ $\mathbf{P}_{source} = \mathbf{P}_{dest}$
Species transport	$D \nabla^2 C = \nabla C \cdot \mathbf{u}$	$-D \nabla C \cdot \mathbf{n} = r$	$flux = C_{in} u_{in}$	$-(\partial C) / (\partial z) = 0$	$C_{source} = C_{dest}$

along z direction indicate an individual CNT ($\sim 100\text{-}\mu\text{m}$ in length) is randomly-oriented in the x - y plane. In the model, the CNT are assumed to be randomly-distributed, similar diameter circular slices in the x - z plane to reduce computation time. These assumptions have a negligible effect on the simulation results (discussion in SI). Since the CNT are closely packed in the x - z plane, the 2D model geometry width was set to be 8.5 times the tube diameter and to have periodic boundary conditions in the x -direction for a representative presentation of the entire width to reduce computation time. The total number of CNT in the model is calculated by the CNT surface area to filter volume ratio and the geometric area of the model domain (calculation in SI).

4.1.2. Hydraulic field model

The hydraulic field within the 2D CNT filter (Fig. 3a) is laminar (Reynolds number (R) = 1.6×10^{-6}). The steady state fluid

velocity field can be numerically solved using the 2D Navier–Stokes equation and mass conservation of an incompressible fluid, Eqs. (1) and (2), respectively:

$$\rho \frac{D\mathbf{u}}{Dt} = -\nabla p + \rho \mathbf{g} + \mu \nabla^2 \mathbf{u} \quad (1)$$

$$\nabla \cdot \mathbf{u} = 0 \quad (2)$$

where \mathbf{u} is the velocity vector, $\rho = 1.0 \text{ g cm}^{-3}$ is the density of water, p is the pressure in Pa, \mathbf{g} (9.8 m s^{-2}) represents gravity, and $\mu = 8.9 \times 10^{-4} \text{ Pa s}$ is the dynamic viscosity of water at 25 °C. The flow field boundary conditions are summarized in Table 2: the average influent flow rate ($u_{in} = 70.8 \times 10^{-6} \text{ m s}^{-1}$) is the domain inlet boundary condition (green Fig. 3a), the no-slip condition is used at CNT electrode surfaces (black), and a periodic boundary condition is applied at the sides (purple) of the model geometry.

4.1.3. Species transport model

The fluid velocity field is the initial input for calculating the target molecule concentration field by the convection–diffusion equations, Eqs. (3) and (4):

$$D\nabla^2 C = \nabla C \cdot \mathbf{u} \text{ in the bulk solution} \quad (3)$$

$$-D\nabla C \cdot \mathbf{n} = r \text{ on the electrode surface} \quad (4)$$

where $D = 8.5 \times 10^{-9} \text{ m}^2 \text{ s}^{-1}$ is the estimated diffusion coefficient for methyl orange, [11] \mathbf{n} is the normal vector to the CNT cylinder surface, C is the target molecule concentration in mol m^{-3} , and r is the reaction rate in $\text{mol m}^{-2} \text{ s}^{-1}$. The movement of a fluid through a porous material may give rise to mechanical mixing resulting in a greater effective diffusivity. However, in this study the fluid velocity is extremely low such that ordinary diffusion dominates i.e., the flow rate would need to be increased 4 orders of magnitude to drive advective dispersion. Detailed discussion is available in SI. The boundary condition at domain inlet is the influent molar flux ($C_{\text{in}} \times u_{\text{in}}$) and a periodic concentration field is assumed for the left and right boundaries. The summary of the governing equations and boundary conditions for the species transport model can be found in Table 2. Detailed information on COMSOL model construction, simulation, and boundary condition selection are available in SI.

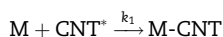
4.1.4. MO electrochemical filtration mechanism

The organic electrochemical filtration reaction mechanism [11] follows a multi-step process:

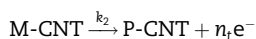
(R0) mass transport to the electrode surface,

Convection–Diffusion; Eqs. (3) and (4)

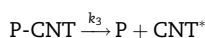
(R1) adsorption to the electrode surface,



(R2) direct electron transfer and molecular transformation,



(R3) and oxidation product desorption,



where CNT^* is a vacant reactive site, M is the reactant, in this case MO, P is the oxidation product, and M-CNT and P-CNT are adsorbed species, n_t is the total number of electron transferred per molecule. In regards to R1, negatively-charged MO adsorption will be increased on a positively-charged CNT anode. If the product is negatively-charged, the same electrostatic interaction may lead to slow product desorption blocking electron-transfer sites. Product readsorption will be embedded in the desorption rate (slower assuming no readsorption). The highest anode potential used in the MO experiments was 0.9 V, much lower than the aromatic ring cleavage potential 2.1 V [32], thus all MO electrooxidation products will be aromatic and have similar strong interactions with a CNT surface.

Rate constants of MO adsorption, electron transfer, and product desorption are k_1 , k_2 , and k_3 , respectively. The surface area normalized reaction rate r ($\mu\text{mol m}^{-2} \text{ s}^{-1}$) can be expressed by:

$$r = k_2 \omega \theta_M \quad (5)$$

where θ_M is the MO fractional surface coverage and ω is the absolute surface reactive site density. The electron transfer rate constant, k_2 , is determined by the Butler–Volmer relation [33], Eq. (6):

$$k_2 = A e^{n\alpha f(E-E_0)} \quad (6)$$

where A ($\text{m}^2 \text{ s}^{-1}$) is the pre-exponential factor, n is the number of electrons transferred in the rate determining step, α is the transfer coefficient, $f = F/RT$ where $F = 96,500 \text{ C mol}^{-1}$ is Faraday's constant, $R = 8.314 \text{ J K}^{-1} \text{ mol}^{-1}$ is the gas constant, and $T = 298 \text{ K}$ is the temperature, E denotes the anode potential, and E_0 is the standard reduction potential. The standard MO reduction potential is a function of pH ($E_0 = 0.3 \text{ V}$ (vs. Ag/AgCl) at $\text{pH}_{\text{in}} = 7$) [34].

The evolution of surface MO (θ_M) and product (θ_P) coverage is described by the following mass balance Eqs. (7) and (8), respectively:

$$\frac{d\theta_M}{dt} = k_1 C_M \omega (1 - \theta_M - \theta_P) - k_2 \omega \theta_M \quad (7)$$

$$\frac{d\theta_P}{dt} = k_2 \omega \theta_M - k_3 \theta_P \omega \quad (8)$$

where C_M denotes the MO concentration in the near CNT surface solution. Assuming steady-state for Eqs. (7) and (8), solving for θ_M , and substituting θ_M into Eq. (5), we receive the electrooxidative reaction rate, r , at the electrode surface, Eq. (9):

$$r = \frac{k_1 k_2 C_M \omega}{k_1 C_M + \frac{k_2}{k_3} k_1 C_M + k_2} = \frac{k_1 A e^{n\alpha f(E-E_0)} C_M \omega}{k_1 C_M + \left(\frac{k_1 C_M}{k_3} + 1\right) A e^{n\alpha f(E-E_0)}} \quad (9)$$

The electrochemical filtration model will be calibrated, validated, and discussed in the following sections.

4.2. Results and discussion

4.2.1. Influent concentration and anode potential dependent kinetics

Electrooxidative MO filtration experiments were completed with an anodic A-CNT network. The concentration change ($\Delta C = C_{\text{in}} - C_{\text{out}}$) between influent and effluent as a function of influent concentration (C_{in}) was measured at anode potentials of 0.45, 0.6, and 0.7 V and is presented in Fig. 4a as open and closed symbols, where the closed symbols are used to calibrate the model and the open symbols to validate the model. The ΔC value first increases with increasing C_{in} because of enhanced mass transport and adsorption kinetics and plateaus due to electron transfer limitations. The threshold concentrations $C_T(E)$ for electron transfer rate plateau increases with increasing anode potential E : $C_T(0.45 \text{ V}) = 17 \mu\text{M} < C_T(0.6 \text{ V}) = 2000 \mu\text{M} < C_T(0.7 \text{ V}) = 4500 \mu\text{M}$, and the plateau height, ΔC , can be used to calculate the k_2 in Eqs. (6) and (9).

For the second set of experiments, the ΔC is measured over a range of anode potentials (0.3–0.9 V) at fixed C_{in} of 300 μM and 875 μM , Fig. 4b, where the symbols are experimental data points (solid to calibrate and open to validate). A similar trend is observed for potential dependent ΔC i.e., ΔC first increases due to an increasing electron transfer rate then plateaus due

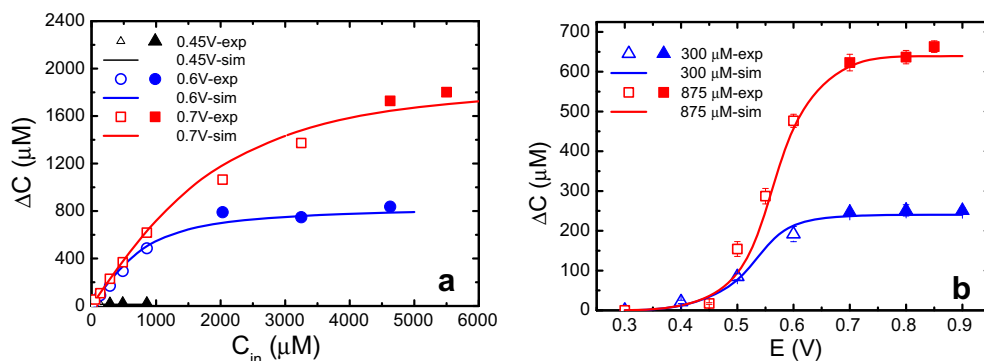


Fig. 4 – Simulated and experimental influent-to-effluent MO concentration change. Concentration change, $\Delta C = C_{in} - C_{out}$, of MO during electrochemical filtration as a function of (a) influent concentration and (b) anode potential. Symbols are experimental measurements: solid to calibrate and open to validate. The electrochemical filtration was carried out with 100 mM Na_2SO_4 as electrolyte and a flow rate $J = 3 \text{ mL min}^{-1}$. Solid curves are model simulation results generated by COMSOL. The kinetic parameters used in simulations are $A\omega = 5.21 \times 10^{-6} \mu\text{mol m}^{-2} \text{ s}^{-1}$, $n\alpha = 0.774$, $k_1\omega = 1.2 \times 10^{-7} \text{ m s}^{-1}$, $k_3\omega = 0.0696 \mu\text{mol m}^{-2} \text{ s}^{-1}$. (A color version of this figure can be viewed online.)

to mass transport limitations likely due to adsorption rather than convection limitations. The mass transport limited regime occurs at 0.6 V for $C_{in} = 300 \mu\text{M}$ and at 0.7 V for $C_{in} = 875 \mu\text{M}$ and the plateau height can be used to calculate the sorption kinetic parameters (k_1 and k_3) in Eq. (9).

4.2.2. Kinetic Parameters Calculation

Kinetic parameters for MO adsorption (k_1), electron transfer (k_2 , $A\omega$, $n\alpha$), and product desorption (k_3) are calculated using closed symbol data (Fig. 4) to calibrate the model. The density of reactive sites (ω) and number of electrons transferred in the rate determining step (n) are difficult to determine individually and thus are determined in combination with the other constants e.g., $A\omega$, $n\alpha$, and, $k_3\omega$. At high influent MO concentrations, Eq. (9) reduces to Eq. (10):

$$\lim_{C_M \rightarrow \infty} r = \frac{A\omega e^{\frac{n\alpha F}{RT}(E-E_0)}}{1 + \frac{A\omega e^{\frac{n\alpha F}{RT}(E-E_0)}}{k_3\omega}} \quad (10)$$

where r corresponds to the maximum reaction rate in the electron transfer limited regime and is calculated from the ΔC plateau values by Eq. (11):

$$r = \frac{J\Delta C}{S} \quad (11)$$

where r has units of $\mu\text{mol m}^{-2} \text{ s}^{-1}$, S stands for total CNT filter surface area (1.47 m^2), ΔC is the plateau value in $\mu\text{mol m}^{-3}$, and J is $5.0 \times 10^{-8} \text{ m}^3 \text{ s}^{-1}$. From Eq. (11) and Fig. 4a, the electron transfer limited reaction rates (r) are 0.45 V ($4.76 \times 10^{-4} \mu\text{mol m}^{-2} \text{ s}^{-1}$) \ll 0.6 V ($2.70 \times 10^{-2} \mu\text{mol m}^{-2} \text{ s}^{-1}$) $<$ 0.7 V ($6.46 \times 10^{-2} \mu\text{mol m}^{-2} \text{ s}^{-1}$). The kinetic parameters: $A\omega = 5.21 \times 10^{-6} \mu\text{mol m}^{-2} \text{ s}^{-1}$, $n\alpha = 0.774$, and $k_3\omega = 0.0696 \mu\text{mol m}^{-2} \text{ s}^{-1}$, were solved with Matlab using the anode potential (E), electron transfer limited rates, and Eq. (10). The $n\alpha$ value is the number of electrons transferred in the rate-determining step, n , multiplied by the charge transfer coefficient, α . The latter is typically in the range of 0.3–0.7, thus n here is likely 1 or 2 and consistent with the literature i.e., although MO electrooxidation is a multi-electron transfer, the elementary rate-determining electron-transfer is the initial one-electron transfer [35].

For the anode potential dependent experiments (Fig. 4b), the data points marked with closed symbols denote the adsorption rate limited ΔC plateau and were used to calculate the MO adsorption rate constant ($k_1\omega$) and product desorption rate constant ($k_3\omega$). At high anode potentials, Eq. (9) reduces to:

$$\lim_{E \rightarrow \infty} r = \frac{k_1 C_M \omega}{\frac{k_1 C_M \omega}{k_3 \omega} + 1} \quad (12)$$

where C_M is the average concentration within the filter and is calculated assuming concentration decreases linearly from the inlet of the diffusion layer to the filter outlet and that C_M is the concentration in the middle of the filter. Given that the filter thickness is $l = 83 \mu\text{m}$ and assuming the bulk concentration begins to decrease at $\delta = \sim 200 \mu\text{m}$ prior to entering the filter [11] and a linearly decreasing concentration profile, C_M can be approximated by Eq. (13):

$$C_M = \frac{(l/2)C_{in} + (l/2 + \delta)C_{out}}{l + \delta} \quad (13)$$

From Eqs. (11) and (12), the adsorption limited reaction rates (r) are 300 μM ($8.3 \times 10^{-3} \mu\text{mol m}^{-2} \text{ s}^{-1}$) $<$ 875 μM ($2.21 \times 10^{-2} \mu\text{mol m}^{-2} \text{ s}^{-1}$) and $k_1\omega$ is determined to be $1.2 \times 10^{-7} \text{ m s}^{-1}$.

COMSOL Multiphysics V 4.2 was used to simulate the coupled hydraulics, species transport, and electrochemical reaction using a finite element method. In the finite element model, nanotubes are simplified as voids with reactive surfaces in the fluid domain. The solution domain is discretized into approximately 200,000 (value is geometry dependent) first order triangular elements and at least 8 boundary layer elements are inserted around the voids (around 56,000 quadrilateral elements in total) for finer resolution of the near surface processes. The COMSOL simulation first determines the hydraulic field that is then used as input together with the above kinetic parameters to simulate the 2D concentration field. The simulated hydraulic field is displayed in Fig. S9 and discussion is available in the SI.

4.2.3. Spatial concentration field and effluent concentration prediction

A simulation of the 2D concentration field for $C_{in} = 300 \mu\text{mol L}^{-1}$ and $E = 0.6 \text{ V}$ is displayed in Fig. 5a. Due to the high model aspect ratio of 8000, the geometry is straight and narrow, so magnified insets are plotted for: the domain inlet, the center of CNT filter and domain outlet. The color bar on the right denotes concentration in mol m^{-3} , with red highest (0.3 mM) and dark blue lowest (0.074 mM). The simulated average MO concentration profile along the direction of the flow is displayed in Fig. 5b. Prior to entering the CNT filter, the MO concentration decreases from 300 to $140 \mu\text{M}$, accounting for 71% of the total concentration decrease. The remaining 29% of the concentration decrease occurred inside the CNT filter. Interestingly, the simulation indicates that the majority of the absolute concentration drop occurs before the filter bed. The filter effluent concentration profile rapidly flattens as expected for a direct surface electrooxidation process.

The quantitative electrochemical filtration model was validated by simulating over the whole range of Fig. 4a and b and the results were plotted as solid lines. It is of note that in both Fig. 4a and b, the simulated effluent target molecule concentrations (lines) agree well with the experimental measurements (points) under all conditions. For example, the simulation correctly describes not only the increasing trend of the reaction rate with influent concentration, but also the position and height of electron transfer limited plateau.

In summary, the quantitative reactive transport model accurately simulated the effluent concentration of the strongly-sorbing, multi-electron transfer methyl orange during electrooxidative filtration as a function of both influent concentration and anode potential. To evaluate the reactive transport model in terms of varying target species physical chemical properties and varying CNT physical chemical properties, the following sections will discuss the electrooxidative filtration experiments and simulation of the non-adsorbing, single-electron-transfer ferrocyanide by five different CNT networks.

5. Ferrocyanide electrooxidative filtration kinetics

Since the overall ferrocyanide electrooxidative filtration mechanism is simpler than methyl orange i.e., single-electron transfer and negligible adsorption, more emphasis can be placed on examining the effects of individual CNT properties. Five different individual CNT of varying specific surface area and surficial oxygen content (Table 1) were used as porous flow-through anodes to investigate the effect of the CNT sp^2 conjugated sidewall and oxy-defect tip reactive sites on the overall electrooxidation kinetics.

5.1. Influent concentration dependent ferrocyanide electrooxidation kinetics

Experiments were completed to examine the ferrocyanide electrooxidation kinetics as a function of influent concentration ($C_{in} = 0.1$ to 35 mM), anode potential ($E = 0.15$ (black), 0.2 (red), 0.3 (blue), and 0.4 V (pink)), and specific CNT anode (A–E) with the steady-state effluent Fe(III) concentrations ($C_{\text{Fe(III)}}$) presented as open squares in Fig. 6. For all experiments, the background electrolyte was $1 \text{ M Na}_2\text{SO}_4$ to minimize electromigration and the flow rate was 3 mL min^{-1} . The electrooxidation kinetics for all CNT increased with increasing anode potential. At lower potentials, 0.15 and 0.2 V , the $C_{\text{Fe(III)}}$ first increases with increasing influent concentration due to enhanced mass transport, but eventually levels off due to electron transfer rate limitations, similar to the MO experiments. The threshold concentration for reaction rate plateaus occur at $C_{in} = 5$ – 10 mM for 0.15 V , and 10 – 17 mM for 0.2 V . Since mass transport/adsorption effects are minimal, the plateau height can be used to calculate the electron transfer kinetic parameters. The plateau $C_{\text{Fe(III)}}$ for the A-CNT, B-CNT, C-CNT, D-CNT, and E-CNT at 0.15 V were 1.21 , 0.6 , 0.45 , 0.33 , and 0.7 mM , respectively, and at 0.2 V were 5.91 , 2.72 , 2.39 , 1.48 , and 3.5 mM , respectively. In contrast, at 0.3 and 0.4 V , the electron transfer limited regime was never observed either because the regime was beyond the experimental C_{in}

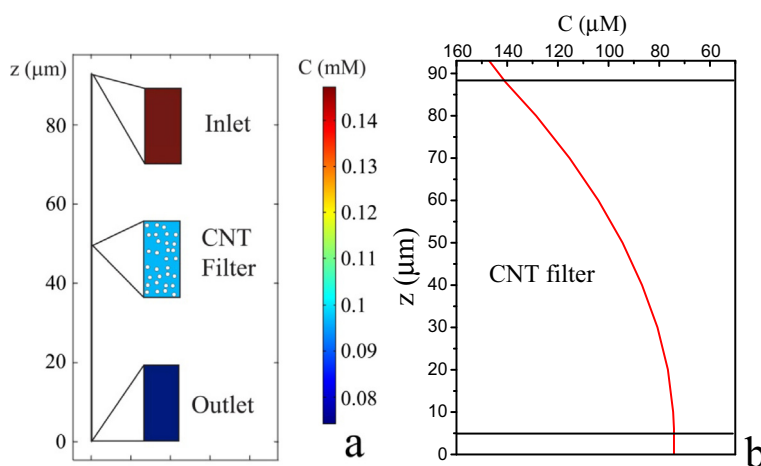


Fig. 5 – Simulated MO concentration electrochemical filter depth profile. (a) Spatial concentration field with geometry with red color being highest concentration, $300 \mu\text{M}$ and blue color being lowest concentration, $74.2 \mu\text{M}$ and (b) average concentration along flow direction showing the CNT filter from $z = 5$ to $88 \mu\text{m}$. Simulations are generated by COMSOL and conditions are $C_{in} = 300 \mu\text{M}$, inlet velocity $u_{in} = 7.08 \times 10^{-5} \text{ m s}^{-1}$, and $E = 0.6 \text{ V}$. (A color version of this figure can be viewed online.)

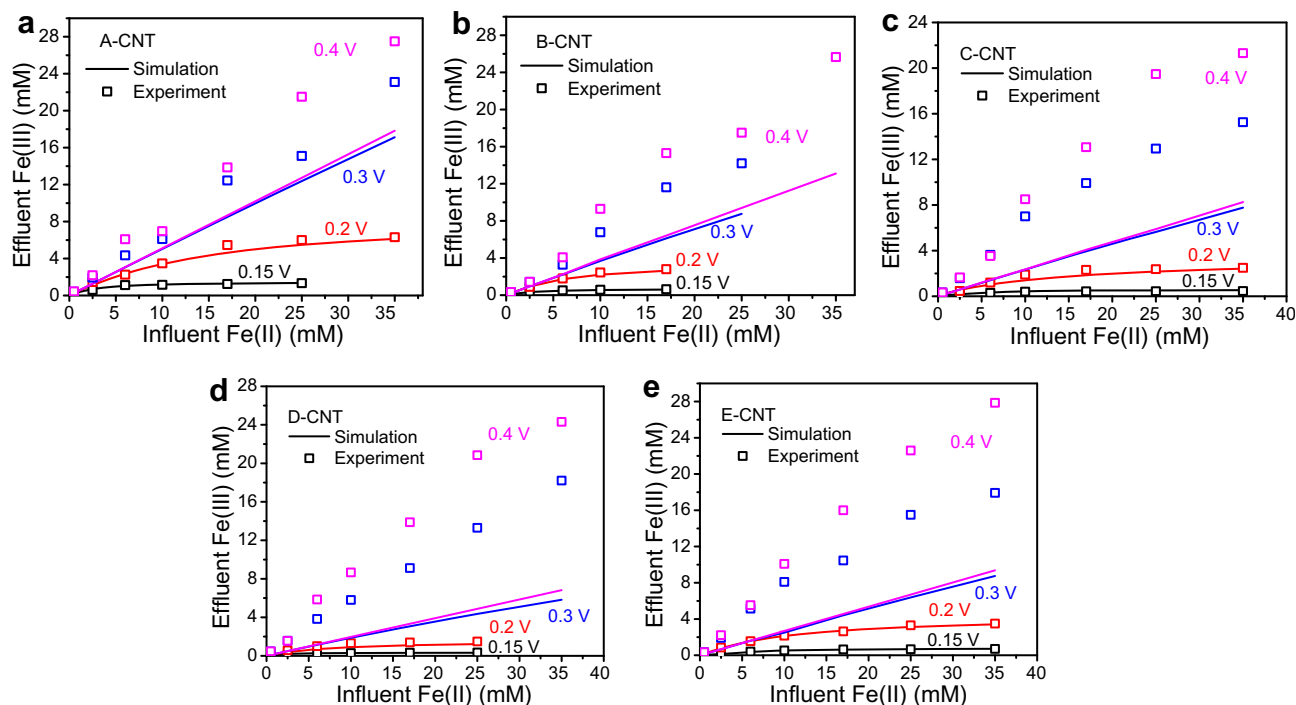


Fig. 6 – Experimental and simulated effluent Fe(III) concentration during ferrocyanide electrooxidative filtration. The oxidation product concentration Fe(III) during electrochemical filtration with (a) A-CNT, (b) B-CNT, (c) C-CNT, (d) D-CNT, and (e) E-CNT. Symbols are experimental measurements and solid lines were model predictions generated by COMSOL considering only sidewall sites. The electrochemical filtration was carried out with 1 M Na₂SO₄ as electrolyte and a flow rate of $J = 3 \text{ mL min}^{-1}$. The kinetic parameters used in simulations are listed in Table 3. (A color version of this figure can be viewed online.)

range or another electron transfer reaction mechanism was activated.

5.2. Ferrocyanide electrooxidative filtration modeling approach

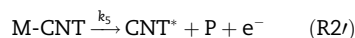
5.2.1. Geometry, hydraulic field, and species transport

A similar modeling approach to methyl orange was used for ferrocyanide electrooxidative filtration. The model geometry consists of a 5- μm headspace, a porous CNT filter anode with specific CNT diameter, thickness, and tube number density that were calculated with the specific CNT physical parameters (Table 1), and finally a 5- μm effluent space. The detailed calculation of the CNT number density is available in the SI and the domain width was set to be 8.5 times the tube diameter. The diffusion coefficient of ferrocyanide is $6.67 \times 10^{-6} \text{ cm}^2 \text{ s}^{-1}$ [36]. The hydraulics, Eqs. (1) and (2), and species transport, Eqs. (3) and (4), were the same as for methyl orange (Table 2 for governing equations and boundary conditions). The primary difference in the ferrocyanide model is the reaction mechanism since sorption is negligible.

5.2.2. Ferrocyanide electrochemical reaction mechanism

Previous CV studies investigating the nature of CNT electrochemically-active sites [28,31] have indicated that CNT sp² sidewalls and/or defect tips (Fig. 1) may be active and the

relative activity depends on the target molecule properties. For MO, a one-site model accurately described the kinetics, thus no information could be obtained regarding the dominant CNT reactive sites. For the ferrocyanide electrooxidation model, a one-site model was initially applied. The mechanism and kinetics were similar (R1, R2, and R3), with M = ferrocyanide and P = ferricyanide. The corresponding kinetic coefficients are denoted k_4 , k_5 , and k_6 for ferrocyanide in place of k_1 , k_2 , and k_3 for MO. Since ferrocyanide is non-adsorbing, desorption is assumed to be very fast and happens immediately after electron transfer, thus R2 and R3 are combined into a single step, R2':



The surface area normalized reaction rate is given by Eqs. (5) and (6), with a ferrocyanide standard potential of $E^0 = 0.134 \text{ V}$ (vs. Ag/AgCl) [37]. Similar to Eq. (7), the ferrocyanide surface coverage can be described by the following mass balance equation:

$$\frac{d\theta_M}{dt} = k_4 C_M \omega (1 - \theta_M) - k_5 \omega \theta_M \quad (14)$$

where C_M denotes the ferrocyanide concentration in the near CNT surface solution. Applying the steady-state condition to θ_M in Eq. (14), solving for θ_M , and then substituting into Eq. (5), we receive the ferrocyanide surface area normalized reaction rate expression, Eq. (15):

$$r = \frac{k_5 \omega k_4 \omega C_M}{k_4 \omega C_M + k_5 \omega} = \frac{A \omega e^{\frac{\alpha F}{RT}(E-E_0)} k_4 C_M}{k_4 C_M + A e^{\frac{\alpha F}{RT}(E-E_0)}} \quad (15)$$

Comparison of the surface area normalized reaction rates for ferrocyanide (Eq. (15)) to MO (Eq. (9)), it is noted that Eq. (15) is a special case of Eq. (9), where $k_6 \gg k_4$ such that k_4/k_6 vanishes and desorption never limits the overall reaction. The electron transfer limited reaction rate is given in Eq. (16) and is reached at both 0.15 and 0.2 V:

$$\lim_{C_{\text{Fe(III)}} \rightarrow \infty} r = A \omega e^{\frac{\alpha F}{RT}(E-E_0)} \quad (16)$$

5.2.3. Reactive site identification and kinetic parameter calculation

If a second CNT reactive site does become active at higher anode potentials, questions arise to the identity of the two sites (sp^2 sidewall vs defect tips) and the potential-dependent relative contribution of each site. Anode potential dependent electron transfer limited reaction rates, r_0 (mol s^{-1}), were calculated by Eq. (17) using the Fe(III) plateau values for 0.15 and 0.2 V, and the highest $C_{\text{Fe(III)}}$ values for 0.3 and 0.4 V where no plateau was observed:

$$r_0 = J C_{\text{Fe(III)}} \quad (17)$$

The electron transfer limited or maximum reaction rates (mol s^{-1}) at 0.15, 0.2, 0.3, and 0.4 V were plotted in Fig. 7a as a function of total anode surface area. There is a linear relationship (solid lines) between the total reaction rate and the surface area of the anode for 0.15 and 0.2 V with $R^2 > 0.99$ indicating a homogeneous reactive site distribution on the CNT

sidewalls at these potentials. In contrast, there is no correlation between reaction rate and total surface area at the higher anode potentials of 0.3 and 0.4 V suggesting a second CNT reactive site that is not homogeneously distributed has been activated.

To complete this comparison, the kinetic parameters for ferrocyanide adsorption ($k_4 \omega$) and electron transfer ($k_5 \omega$, $A \omega$, α) must be determined. However, the mass transport limited reaction rate plateau values for the one-site model cannot be determined since the anode potentials necessary activate a second reaction. Thus, the adsorption ($k_4 \omega$) and electron transfer ($k_5 \omega$) kinetic parameters were estimated using only the data at 0.15 and 0.2 V (Table S1). The $k_5 \omega$ values at anode potentials 0.15 and 0.2 V (Fig. 7b) were used to calculate the $A \omega$ and α values by the Butler–Volmer relation (Eq. (6)). The $k_4 \omega$ value was the average of the 0.15 and 0.2 V results. The estimated $k_4 \omega$, $A \omega$, and α values for S-sites of all five CNT anodes are summarized in Table 3.

The $k_5 \omega$ values are plotted against the CNT anode surface oxygen content in Fig. 7b. The surface oxygen ratio is related to the number of CNT oxygen defect sites largely present at the tips. At 0.15 and 0.2 V, the surface oxygen ratio has no effect on the $k_5 \omega$ values. In contrast, at 0.3 and 0.4 V there is an effect suggesting the second reaction site is related to CNT surficial oxygen. To test this hypothesis, a two-site model will be evaluated towards distinguishing the kinetic contribution of sp^2 sidewall (S-sites) and the oxy-defect tip (T-sites) assuming that the S-sites are dominant at 0.15 and 0.2 V and that the T-sites contribute at 0.3 and 0.4 V.

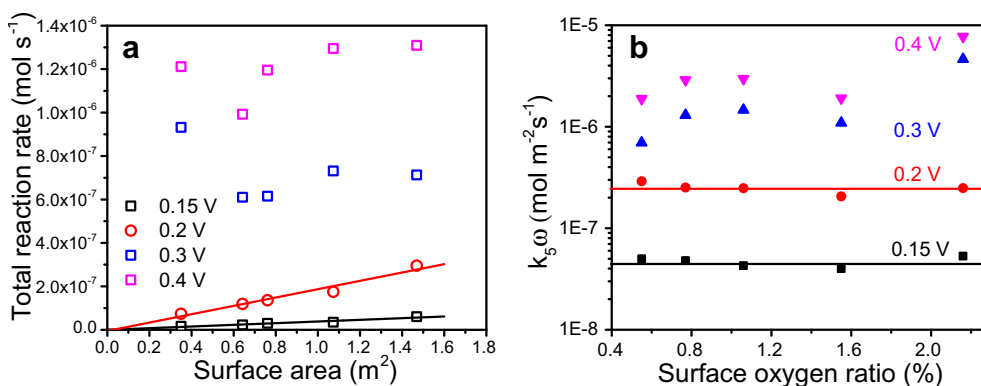


Fig. 7 – Ferrocyanide electrooxidation kinetics versus total surface area and surface oxygen ratio. (a) Maximum total reaction rate (mol s^{-1}) as a function of anode surface area. The open squares for 0.15 (black) and 0.2 V (red) are electron transfer limited reaction rates. Then open squares for 0.3 (blue) and 0.4 V (pink) are maximum reaction rates measured under experimental conditions. The straight lines are linear fittings for 0.15 (black) and 0.2 V (red). (b) $k_5 \omega$ values at anode potentials 0.15 (black), 0.2 (red), 0.3 (blue), and 0.4 V (pink). Horizontal lines denote the average values at 0.15 and 0.2 V. (A color version of this figure can be viewed online.)

Table 3 – Summary of S-site kinetic parameters for ferrocyanide model simulation.

CNT anode	A	B	C	D	E
$A \omega$ ($\text{mol m}^{-2} \text{s}^{-1}$)	2.85×10^{-8}	2.82×10^{-8}	2.44×10^{-8}	3.24×10^{-8}	2.37×10^{-8}
α	0.90	0.85	0.90	0.79	0.84
$k_4 \omega$ (m s^{-1})	2.61×10^{-8}	3.60×10^{-8}	2.10×10^{-8}	3.54×10^{-8}	1.63×10^{-8}

5.3. Results and discussion

5.3.1. S-site Electrooxidation Kinetics

Numerical simulation of ferrocyanide electrooxidation was completed for all CNT at the same influent concentration/anode potential combination as Fig. 6 to predict effluent ferricyanide concentrations. The ferricyanide simulation results at 0.15, 0.2, 0.3, and 0.4 V were plotted as solid lines in Fig. 6a–e, for A-CNT, B-CNT, C-CNT, D-CNT, and E-CNT, respectively. The simulation accurately described the increase of reaction rate with influent concentration and anode potential as well as the position and height of the electron transfer limited plateau at 0.15 and 0.2 V, but significantly underestimated the kinetics at 0.3 and 0.4 V. Comparison of the experimental and simulation results indicates there are two distinct CNT reaction sites with S-sites dominant at lower potentials and T-sites activated at higher potentials. Although the second site has a higher ferrocyanide electrooxidation overpotential, the difference between experimental and simulation kinetics at ≥ 0.3 V indicates that it also has faster electron transfer kinetics.

5.3.2. T-site electrooxidation kinetics

The T-site contribution (light bars) to electrooxidation was estimated by the difference between experimental and simulation effluent ferricyanide concentration results (Fig. 6) and plotted with the contribution of S-site electrooxidation (dark bars) at 0.3 (green) and 0.4 (blue) V in Fig. 8a–e for A-CNT,

B-CNT, C-CNT, D-CNT, and E-CNT, respectively. Generally, for all CNT, faster kinetics was observed for both S- and T-sites with increasing influent ferrocyanide concentration and anode potential. For example, in Fig. 8a the ferrocyanide electrooxidation via T-sites increased from 1.3 mM at $C_{in} = 6$ mM to 6.0 mM at $C_{in} = 35$ mM when $V_{anode} = 0.3$ V, and increased further to 9.6 mM at $C_{in} = 35$ mM when $V_{anode} = 0.4$ V. However, the fractional contribution of the S- and T-sites with increasing anode potential varied for each individual CNT type. For instance, the fractional contribution of T-sites to electrooxidation for the A-CNT (lowest O content; 0.55%) at $C_{in} = 25$ mM was 0 at 0.2 V, increased to 0.19 at 0.3 V, and increased again to 0.41 at 0.4 V. For the D-CNT (highest O content; 2.17%), the fractional T-site contribution was significantly greater, increasing to 0.67 at 0.3 V and 0.77 at 0.4 V even though the $S_{(A-CNT)} = 4 \times S_{(D-CNT)}$, indicating that the higher potential T-sites are likely the oxy-defect sites at the CNT tips. Although the T-sites had a slightly higher ferrocyanide electrooxidation overpotential than the S-sites (+66 mV), the T-site electrooxidation kinetics increase with anode potential was greater than the S-sites. This result is consistent with the ferrocyanide CV study by Gong et al. [31] where an insulating polymer was used to expose only sidewalls (S-CNT) or tips (T-CNT) and a smaller ΔE_p was observed for the T-sites indicating faster electron transfer kinetics. For methyl orange, a one-site model was likely successful due to the T-sites dominating at the higher anode potentials (≥ 0.3 V) used for electrooxidation.

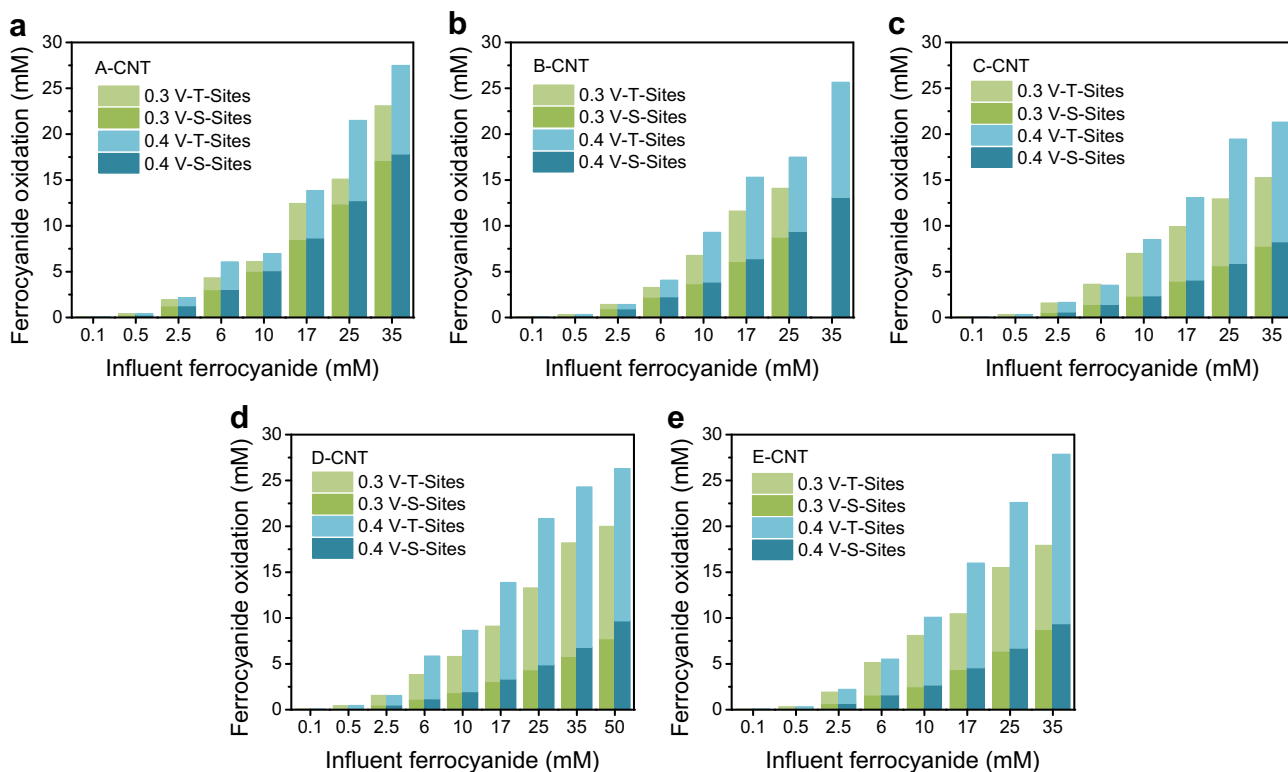


Fig. 8 – Contribution of the S-sites and T-sites to ferrocyanide oxidation various CNT. (a) A-CNT, (b) B-CNT, (c) C-CNT, (d) D-CNT and (e) E-CNT. The ferrocyanide oxidation (mM) is green for 0.3 V and blue for 0.4 V. The dark colors indicate S-site electrooxidation generated by COMSOL simulation and the light colors indicate T-site electrooxidation calculated by the difference between experimental and simulated S-site electrooxidation. (A color version of this figure can be viewed online.)

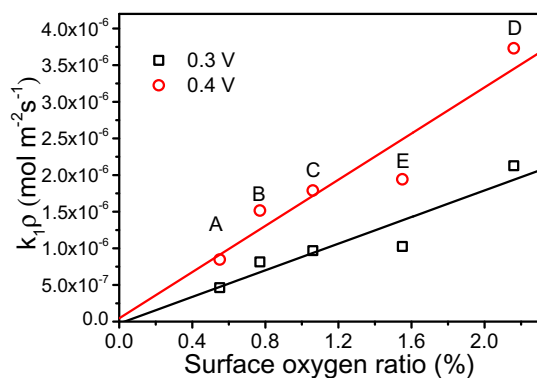


Fig. 9 – T-sites electron transfer kinetics as a function of anode oxygen ratio. The symbols are the T-site electrooxidation data in Fig. 8. The solid lines are linear fittings for 0.3 (black) and 0.4 V (red). (A color version of this figure can be viewed online.)

To further support the CNT electroactive site identification, the T-site electron transfer kinetic parameters are compared to the measured CNT surficial oxygen ratio. It is assumed that the same governing S-site kinetic equations also apply to the T-sites. The T-site $k_5\omega$ values for all CNT networks as a

function of anode potential (0.3 and 0.4 V) were estimated using Eqs. (15), (17) and Fig. 8 through fitting of r to C_M from Eq. (15) and the results are plotted in Fig. S10a and b. The estimated T-site $k_5\omega$ values for the various CNT at 0.3 and 0.4 V were then plotted versus the CNT anode surface oxygen ratio in Fig. 9. The $k_5\omega$ values exhibited a linear relationship with the CNT surface oxygen ratio at both 0.3 V ($R^2 = 0.84$) and 0.4 V ($R^2 = 0.87$) providing further support for the conclusion that the higher overpotential and faster kinetic T-sites are represented by oxy-defects at the CNT tips [31]. In addition the lack of correlation to S and correlation to surficial oxygen supports the assumption that CNT oxy-defects are predominantly located at the CNT tips. The slight deviations of $k_5\omega$ vs. CNT surface oxygen from linearity is likely because the number of surface oxygen atoms may not be perfectly correlated to the number of oxy-defect groups e.g., a hydroxyl group contains 1 O-atom and a carboxylate group contains 2 O-atoms. In conclusion, the ferrocyanide electrooxidation kinetic modeling revealed the CNT networks have two distinct reactive sites of the sp^2 conjugated sidewalls (S-sites) and the oxy-defect tips (T-sites) with the latter having a higher overpotential (+66 mV) and faster electron transfer kinetics.

The anodic onset potential (+0.2–0.3 V vs. Ag/AgCl) observed for the T-sites may be associated with the CNT

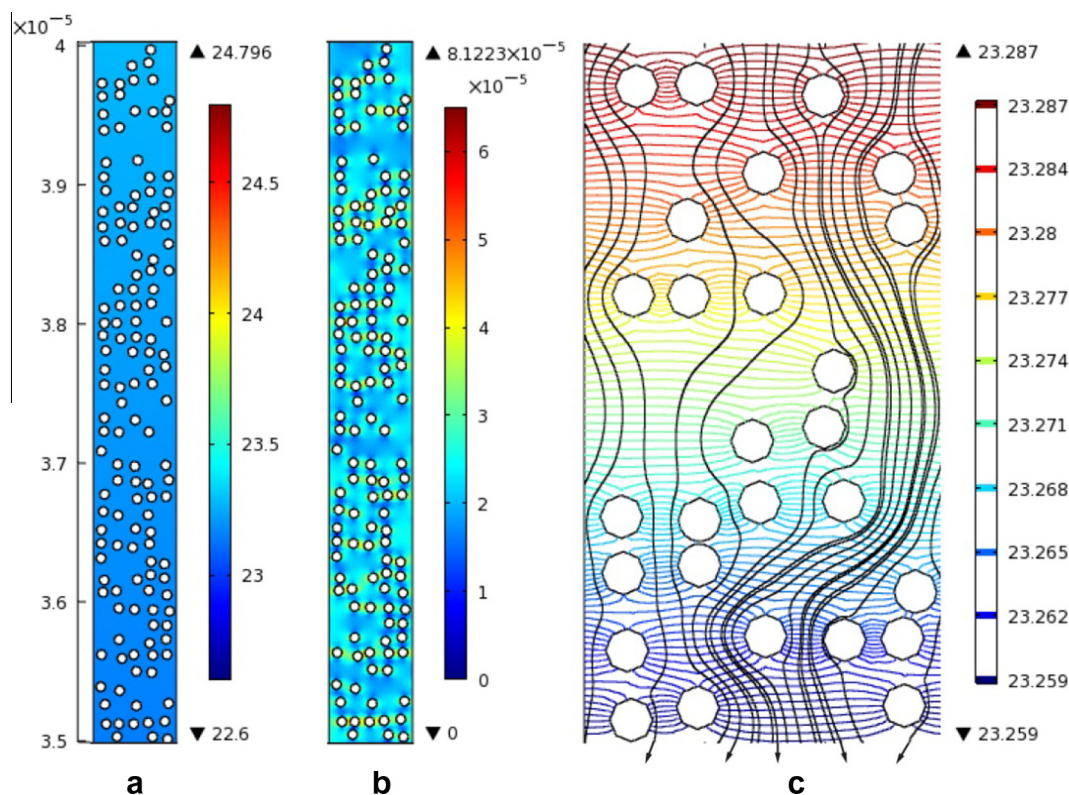


Fig. 10 – Microscopic concentration field, diffusional flux, and streamline simulations for C-CNT. (a) Concentration field, concentration ranging from 23.3 mM on top to 23.2 mM at the bottom, (b) diffusional flux magnitude field, ranging from $4.7 \times 10^{-5} \text{ mol m}^{-2} \text{ s}^{-1}$ (red) to $7 \times 10^{-6} \text{ mol m}^{-2} \text{ s}^{-1}$ (blue). (c) Overlapped concentration contours and streamlines. Concentration contours ranging from 23.259 (blue) to 23.287 μM (red). The streamlines are in black. The representative patterns inside the CNT filter are shown from $z = 35$ to $40 \mu\text{m}$ for (a) and (b), and $z = 39.4$ to $40.6 \mu\text{m}$ for (c). Simulations are generated by COMSOL and conditions are ferrocyanide at $C_{in} = 25 \text{ mM}$, $V_{in} = 7.08 \times 10^{-5} \text{ m s}^{-1}$, and $E = 0.2 \text{ V}$. (A color version of this figure can be viewed online.)

electronic properties. A study on single-walled CNT observed that there was a threshold potential (+0.2 V for metallic and +0.7 V for semiconducting) for transfer of static positive charge to the CNT. Multi-walled CNT are a mixture of metallic (1/3) and semiconducting (2/3) CNT with the metallic tending to dominate electronic properties [38]. The anodic T-site onset potential here may be necessary to activate the oxy-containing defect sites via positive charging prior to electrochemical ferrocyanide oxidation [39].

5.3.3. Single CNT spatial reaction rate distribution

The simulated concentration and diffusional flux fields, Fig. 10a and b, respectively, provide insight into the spatial distribution of mass transport and electrochemical kinetics within the CNT network. The concentration decreased by 0.1 mM (~0.5% of influent concentration) in the direction of the fluid flow after passing through 5- μm of filter depth or had a concentration gradient of 24 $\mu\text{M } \mu\text{m}^{-1}$ in the z-direction. There was minimal concentration gradient in the x-direction with the exception of lines passing through a region near the top/bottom of an individual CNT. There was minimal concentration field variation (~0.01%) on the scale of a single CNT (100 nm) as expected since the simulation conditions are in the electron transfer limited regime i.e., mass transport is sufficient since diffusion is rapid at the nanoscale. The average distance between the CNT is <200 nm and small compared to the filter thickness of ~90 μm . The estimated time for a target molecule to diffuse ~100 nm, the maximum distance to a CNT surface, is 4×10^{-7} s and significantly lesser than the hydraulic residence time of 1.2 s. The homogenous near CNT surface concentration indicates that the spatially distributed reaction rate around an individual CNT perimeter is also homogeneous as expected for a surface area dependent reaction according to Eq. (15).

In contrast, the spatial distribution of the 2D diffusional flux was quite heterogeneous (up to 90%) around an individual CNT perimeter. The diffusional flux is directly proportional to and thus representative of the concentration gradient. Although the absolute concentration difference around a single CNT in Fig. 10a is quite small (~0.01% of bulk concentration), its gradient ($dC/dz = 24 \mu\text{M } \mu\text{m}^{-1}$) is not insignificant due to the extremely small scale (<100 nm). Diffusional fluxes were the lowest (minimum of $7 \times 10^{-6} \text{ mol m}^{-2} \text{ s}^{-1}$) at the CNT top/bottom, in regards to fluid flow, and were the highest (maximum of $7 \times 10^{-5} \text{ mol m}^{-2} \text{ s}^{-1}$) at the sides. The large spatial range of diffusional flux/concentration gradient is due to the hydraulic field patterns. The representative concentration contour under finer resolution and hydraulic streamline simulations are displayed in Fig. 10c. The streamlines were mostly perpendicular to the concentration contours near each single CNT indicating the concentration gradient/diffusional flux is maintained by advection and that the diffusional flux is predominantly in a similar direction to the fluid flow. The fluid stagnation points at the top/bottom of an individual CNT results in slow convective target molecule replenishment; whereas the high fluid velocity near the sides of an individual CNT results in rapid target molecule replenishment, high

concentration gradients, and high diffusional flux. Thus, within the electrochemical CNT network the rate of mass transport can be enhanced up to 10-fold within regions of rapid fluid flow that in turn maintains a high concentration gradient resulting in faster diffusion.

In summary, the electrochemical filter simulation allows for examination of microscopic flux and concentration gradients around an individual CNT that are experimentally difficult to probe.

6. Conclusion

The electrooxidative filtration kinetics of methyl orange and ferrocyanide were investigated by both experiment and simulation. The target molecules were selected to cover a range electrochemical activity; ferrocyanide is non-adsorptive and undergoes a single outer-sphere electron transfer and in contrast MO is strongly adsorptive and undergoes a multi-electron transfer. The physical model used to quantitatively describe the experimental data consists of four primary mechanistic steps: target molecule mass transport, adsorption, and electron transfer as well as product desorption. For methyl orange, a single-site model simulation was able to accurately predict effluent concentrations over a range of solution and electrochemical conditions. For ferrocyanide, the single-site model simulation could only predict effluent concentrations at low anode potentials (≤ 0.2 V) and a two-site model was necessary for prediction at higher anode potentials (≥ 0.3 V). Ferrocyanide electrooxidative filtration was completed using five different individual CNT of varying SSA and O/C ratio. The single site ferrocyanide electrooxidation kinetics correlated well with the SSA of the CNT networks indicating the sp^2 sidewalls were the predominant reaction site at low anode potential. The differential (total – sidewall site) ferrocyanide electrooxidation kinetics correlated well with the O/C ratio of the CNT networks indicating the oxy-tips also contributed at higher anode potentials. The tip differential kinetics had a greater increase with potential than the sidewall kinetics, thus although the sp^2 sidewalls had a lower ferrocyanide electrooxidation overpotential than the oxy-tips, once activated the oxy-tips had faster electrochemical kinetics. Finally, the simulation was used to probe the internal CNT electrode spatial concentration, concentration gradient, and diffusional flux distribution and it was observed that although the concentration is quite homogeneous in x at each depth z, the gradient and diffusional flux can be 10-fold greater at the sides of a CNT as compared to the top/bottom due to convective replenishment.

Acknowledgements

We thank Harvard's Center for Nanoscale Systems for SEM, TEM, and XPS. We thank Harvard's Material Research Science and Engineering Center for TGA. H.L. thanks Harvard University Center for the Environment's Graduate Consortium for funding. We thank Harvard Office of Technology Development for funding.

Appendix A. Supplementary data

Supplementary data associated with this article can be found, in the online version, at <http://dx.doi.org/10.1016/j.carbon.2014.09.009>.

REFERENCES

- [1] Yang J, Wang J, Jia JP. Improvement of electrochemical wastewater treatment through mass transfer in a seepage carbon nanotube electrode reactor. *Environ Sci Technol* 2009;43(10):3796–802.
- [2] Vecitis CD, Gao GD, Liu H. Electrochemical carbon nanotube filter for adsorption, desorption, and oxidation of aqueous dyes and anions. *J Phys Chem C* 2011;115(9):3621–9.
- [3] Brady-Estevéz AS, Schnoor MH, Kang S, Elimelech M. SWNT–MWNT hybrid filter attains high viral removal and bacterial inactivation. *Langmuir* 2010;26(24):19153–8.
- [4] Vecitis CD, Schnoor MH, Rahaman MS, Schiffman JD, Elimelech M. Electrochemical multiwalled carbon nanotube filter for viral and bacterial removal and inactivation. *Environ Sci Technol* 2011;45(8):3672–9.
- [5] Lohner ST, Becker D, Mangold KM, Tiehm A. Sequential reductive and oxidative biodegradation of chloroethenes stimulated in a coupled bioelectro-process. *Environ Sci Technol* 2011;45(15):6491–7.
- [6] Gent DB, Wani AH, Davis JL, Alshawabkah A. Electrolytic redox and electrochemical generated alkaline hydrolysis of hexahydro-1,3,5-trinitro-1,3,5-triazine (RDX) in sand columns. *Environ Sci Technol* 2009;43(16):6301–7.
- [7] Zaky AM, Chaplin BP. Porous substoichiometric TiO₂ anodes as reactive electrochemical membranes for water treatment. *Environ Sci Technol* 2013;47(12):6554–63.
- [8] Wu J, Gerstandt K, Majumder M, Zhan X, Hinds BJ. Highly efficient electroosmotic flow through functionalized carbon nanotube membranes. *Nanoscale* 2011;3(8):3321–8.
- [9] Gonzalez-Garcia J, Montiel V, Aldaz A, Conesa JA, Perez JR, Codina G. Hydrodynamic behavior of a filter-press electrochemical reactor with carbon felt as a three-dimensional electrode. *Ind Eng Chem Res* 1998;37(11):4501–11.
- [10] Gao GD, Vecitis CD. Doped carbon nanotube networks for electrochemical filtration of aqueous phenol: electrolyte precipitation and phenol polymerization. *ACS Appl Mater Interfaces* 2012;4(3):1478–89.
- [11] Liu H, Vecitis CD. Reactive transport mechanism for organic oxidation during electrochemical filtration: mass-transfer, physical adsorption, and electron-transfer. *J Phys Chem C* 2012;116(1):374–83.
- [12] Jiang LY, Wang RX, Li XM, Jiang LP, Lu GH. Electrochemical oxidation behavior of nitrite on a chitosan-carboxylated multiwall carbon nanotube modified electrode. *Electrochem Commun* 2005;7(6):597–601.
- [13] Melitas N, Conklin M, Farrell J. Electrochemical study of arsenate and water reduction on iron media used for arsenic removal from potable water. *Environ Sci Technol* 2002;36(14):3188–93.
- [14] Xiao Y, Rowe AA, Plaxco KW. Electrochemical detection of parts-per-billion lead via an electrode-bound DNAzyme assembly. *J Am Chem Soc* 2007;129(2):262–3.
- [15] Rajkumar D, Kim JG, Palanivelu K. Indirect electrochemical oxidation of phenol in the presence of chloride for wastewater treatment. *Chem Eng Technol* 2005;28(1):98–105.
- [16] Chen J, Cai CX. Direct electrochemical oxidation of NADPH at a low potential on the carbon nanotube modified glassy carbon electrode. *Chin J Chem* 2004;22(2):167–71.
- [17] Ziyatdinova G, Grigor'eva L, Morozov M, Gilmuddinov A, Budnikov H. Electrochemical oxidation of sulfur-containing amino acids on an electrode modified with multi-walled carbon nanotubes. *Microchim Acta* 2009;165(3–4):353–9.
- [18] McCreery RL. Advanced carbon electrode materials for molecular electrochemistry. *Chem Rev* 2008;108(7):2646–87.
- [19] Hou PX, Xu ST, Ying Z, Yang QH, Liu C, Cheng HM. Hydrogen adsorption/desorption behavior of multi-walled carbon nanotubes with different diameters. *Carbon* 2003;41(13):2471–6.
- [20] Banks CE, Davies TJ, Wildgoose GG, Compton RG. Electrocatalysis at graphite and carbon nanotube modified electrodes: edge-plane sites and tube ends are the reactive sites. *Chem Commun* 2005;7:829–41.
- [21] Stephan O, Ajayan PM, Colliex C, Redlich P, Lambert JM, Bernier P, et al. Doping graphitic and carbon nanotube structures with boron and nitrogen. *Science* 1994;266(5191):1683–5.
- [22] Jiang J, Kucernak A. Mass transport and kinetics of electrochemical oxygen reduction at nanostructured platinum electrode and solid polymer electrolyte membrane interface. *J Solid State Electrochem* 2012;16(8):2571–9.
- [23] Logue BA, Westall JC. Kinetics of reduction of nitrobenzene and carbon tetrachloride at an iron-oxide coated gold electrode. *Environ Sci Technol* 2003;37(11):2356–62.
- [24] Pretty SD, Keech PG, Zhang X, Noel JJ, Wren JC. Investigation of interfacial reaction kinetics of I_(aq)⁻ with Ag₂O_(s) on Ag substrate: determining mass transport and surface reaction rates. *Electrochim Acta* 2011;56(6):2754–61.
- [25] Chaplin BP, Schrader G, Farrell J. Electrochemical oxidation of N-nitrosodimethylamine with boron-doped diamond film electrodes. *Environ Sci Technol* 2009;43(21):8302–7.
- [26] Carter KE, Farrell J. Electrochemical oxidation of trichloroethylene using boron-doped diamond film electrodes. *Environ Sci Technol* 2009;43(21):8350–4.
- [27] Zhang D, Deutschmann O, Seidel YE, Behm RJ. Interaction of mass transport and reaction kinetics during electrocatalytic CO oxidation in a thin-layer flow cell. *J Phys Chem C* 2011;115(2):468–78.
- [28] Dumitrescu I, Unwin PR, Macpherson JV. Electrochemistry at carbon nanotubes: perspective and issues. *Chem Commun* 2009;45:6886–901.
- [29] Banks CE, Moore RR, Davies TJ, Compton RG. Investigation of modified basal plane pyrolytic graphite electrodes: definitive evidence for the electrocatalytic properties of the ends of carbon nanotubes. *Chem Commun* 2004;16:1804–5.
- [30] Banks CE, Ji XB, Crossley A, Compton RG. Understanding the electrochemical reactivity of bamboo multiwalled carbon nanotubes: the presence of oxygenated species at tube ends may not increase electron transfer kinetics. *Electroanalysis* 2006;18(21):2137–40.
- [31] Gong KP, Chakrabarti S, Dai LM. Electrochemistry at carbon nanotube electrodes: is the nanotube tip more active than the sidewall? *Angew Chem Int Ed* 2008;47(29):5446–50.
- [32] Gao GD, Vecitis CD. Reactive depth and performance of an electrochemical carbon nanotube network as a function of mass transport. *ACS Appl Mater Interfaces* 2012;4(11):6096–103.
- [33] Liu ZJ, Betterton EA, Arnold RG. Electrolytic reduction of low molecular weight chlorinated aliphatic compounds: structural and thermodynamic effects on process kinetics. *Environ Sci Technol* 2000;34(5):804–11.
- [34] Liu L, Li FB, Feng CH, Li XZ. Microbial fuel cell with an azo-dye-feeding cathode. *Appl Microbiol Biotechnol* 2009;85(1):175–83.

-
- [35] Bard AJ. *Electrochemical methods: fundamentals and application*. 2nd ed. New York: John Wiley & Sons, Inc.; 2001.
- [36] Konopka SJ, McDuffie B. Diffusion coefficients of ferricyanide and ferrocyanide ions in aqueous media using twin-electrode thin-layer electrochemistry. *Anal Chem* 1970;42(14):1741–6.
- [37] Kolthoff IM, Tomsicek WJ. The oxidation potential of the system potassium ferrocyanide–potassium ferricyanide at various ionic strengths. *J Phys Chem* 1935;39(7):945–54.
- [38] Stavarache I, Lepadatu AM, Teodorescu VS, Ciurea ML, Iancu V, Dragoman M, et al. Electrical behavior of multi-walled carbon nanotube network embedded in amorphous silicon nitride. *Nanoscale Res Lett* 2011;6:88.
- [39] Dragin F, Penicaud A, Iurlo M, Marcaccio M, Paolucci F, Anglaret E, et al. Raman doping profiles of polyelectrolyte SWNTs in solution. *ACS Nano* 2011;5(12):9892–7.